AGU ADVANCING EARTH AND SPACE SCIENCE

Water Resources Research

RESEARCH ARTICLE
10.1029/2022WR032633

Unconfined Plunging of a Hyperpycnal River Plume Over a Sloping Bed and Its Lateral Spreading: Laboratory Experiments and Numerical Modeling

H. Shi[1], M. E. Negretti[2], J. Chauchat[2], K. Blanckaert[3], U. Lemmin[1], and D. A. Barry[1]

[1]Ecological Engineering Laboratory (ECOL), Environmental Engineering Institute (IIE), Faculty of Architecture, Civil and Environmental Engineering (ENAC), École Polytechnique Fédérale de Lausanne (EPFL), Lausanne, Switzerland, [2]Université Grenoble Alpes, CNRS, Grenoble INP, LEGI UMR 5519, Grenoble, France, [3]Research Unit Hydraulic Engineering, Institute of Hydraulic Engineering and Water Resources Management, Technische Universität Wien, Vienna, Austria

Key Points:

- Main features of unconfined plunging are investigated experimentally and numerically
- The inflow densimetric Froude number is a primary control parameter for plunging behavior
- Entrainment in unconfined plunging is much larger than in confined plunging

Supporting Information:

Supporting Information may be found in the online version of this article.

Correspondence to:

H. Shi,
haoran.shi@epfl.ch

Citation:

Shi, H., Negretti, M. E., Chauchat, J., Blanckaert, K., Lemmin, U., & Barry, D. A. (2022). Unconfined plunging of a hyperpycnal river plume over a sloping bed and its lateral spreading: Laboratory experiments and numerical modeling. *Water Resources Research*, *58*, e2022WR032633. https://doi.org/10.1029/2022WR032633

Received 20 APR 2022
Accepted 7 AUG 2022

Author Contributions:

Conceptualization: H. Shi, K. Blanckaert
Data curation: H. Shi, M. E. Negretti
Formal analysis: H. Shi
Funding acquisition: D. A. Barry
Investigation: H. Shi
Methodology: U. Lemmin
Project Administration: K. Blanckaert, D. A. Barry
Software: J. Chauchat
Supervision: M. E. Negretti, J. Chauchat, K. Blanckaert, U. Lemmin, D. A. Barry
Writing – original draft: H. Shi, M. E. Negretti
Writing – review & editing: M. E. Negretti, J. Chauchat, K. Blanckaert, U. Lemmin, D. A. Barry

Abstract Hyperpycnal (negatively buoyant) river inflow into lakes and oceans often develops three-dimensional (3D) plunging flow patterns when laterally unconfined. To determine the 3D flow pattern characteristics, laboratory experiments of laterally unconfined plunging on a sloping bed were carried out using salinity to control the density difference. The experiments were complemented by numerical modeling based on a high-resolution computational fluid dynamics model. As is the case for confined plunging plumes, it was found that in unconfined plunging, the inflow densimetric Froude number Fr_{d-0} at the river mouth and the bed slope of the receiving water body β are the dominant control parameters. However, the results documented that the hydrodynamics of laterally unconfined plunging are fundamentally different: The hyperpycnal plume in unconfined configurations forms a triangle on the surface in the plunge zone due to its convergence near the surface and lateral spreading near the bottom. The triangular pattern extends further into the receiving water when Fr_{d-0} increases or the bottom slope decreases. The unconfined entrainment coefficient, which quantifies the amount of ambient water entrained into the plunging plume, also increases with increasing Fr_{d-0}. In general, entrainment is much higher in unconfined than in confined plunging. The plunging densimetric Froude number Fr_{d-p} takes a constant value of ~0.5 in confined plunging, whereas it increases with increasing Fr_{d-0} and can be $\gg 1$ in unconfined plunging. Complex patterns of secondary currents occur in the plunging plume. A low-velocity zone whose size increases with Fr_{d-0} is observed near the centerline above the bed.

1. Introduction

River inflows carry sediments, contaminants, and nutrients into reservoirs, lakes, or oceans (Branch et al., 2020; Lamb et al., 2010; Pope et al., 2022; Scheu et al., 2018). The present paper focuses on river inflows that have a higher density (ρ_0) than the receiving waters (ρ_a), hereinafter referred to as hyperpycnal (negatively buoyant) river inflows. The excess density may result from lower temperatures (Hogg et al., 2013; Spigel et al., 2005), suspended sediments (De Cesare et al., 2001; Kostaschuk et al., 2018; Wright et al., 1986), or both (Best et al., 2005). Understanding how hyperpycnal river inflows transport and how they mix with ambient waters is essential for predicting and modeling the fate of fluvial materials (e.g., dissolved salts, heat, chemicals, biological particles, and sediment) and thus for determining how they will affect water quality, local ecosystems, and morphological evolution.

Upon entering the receiving water body, the hyperpycnal discharge displaces ambient water and then plunges below the surface at the plunge location ($x = x_p$), which is determined by a balance between the momentum of the inflow and the baroclinic pressure resulting from the density difference (e.g., Figure 6.18 of Fischer et al., 1979; see also Figures 1 and 2). After plunging, the hyperpycnal plume transforms into an underflow at distance x_{ud} from the river mouth. Thus, the plunge region can be divided into two parts: from the river mouth to the plunge location ($0 < x \le x_p$) and from the plunge location to the location where the plunging plume has transformed into an underflow ($x_p < x \le x_{\mathrm{ud}}$). The underflow progresses along the bottom boundary (e.g., Kostaschuk et al., 2018) and may detach from the bottom at the level of neutral buoyancy (e.g., Cortés et al., 2014).

Sediment-laden hyperpycnal plumes can cause turbidity currents. If the hyperpycnal plume gradually loses momentum, suspended sediment can settle out (Lamb et al., 2010), which reduces the excess density. On the other hand, the hyperpycnal plume can also pick up sediment from the bottom and thereby increase its excess density,

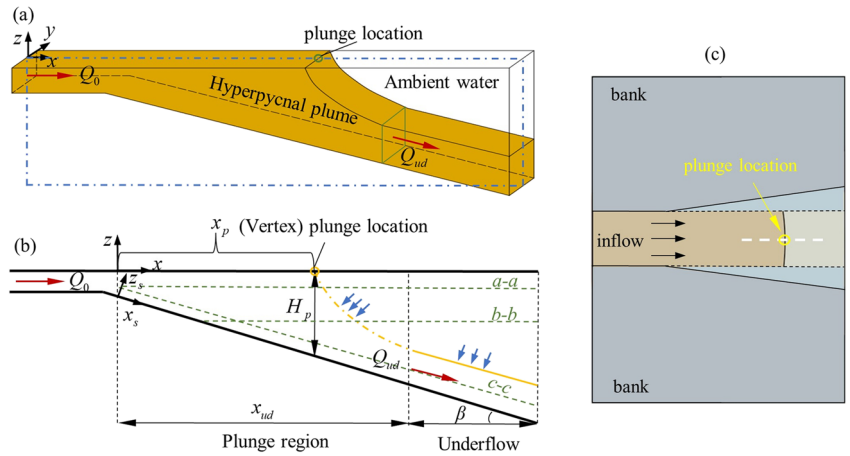

Figure 1. (a) Sketch of the confined plunging process on a sloping bed with inflow discharge Q_0 and underflow discharge Q_{ud}. (b) Sketch of the central plane ($y/B_0 = 0$, B_0 is the width of the inflow) identified by the blue dashed-dotted lined box in panel (a). The orange line indicates the limits of the plunging plume and the blue arrows indicate entrainment. This sketch also describes the central plane of unconfined plunging (Figure 2). The transversal planes passing through (*a-a*, *b-b*, and *c-c*) are the locations of the particle image velocimetry sheets in the laterally unconfined experiments, the results of which are shown in Figure 5. (c) Plan view sketch of the confined plunging process.

potentially leading to self-acceleration (Parker et al., 1986; Sequeiros et al., 2009). Both sediment deposition and pick-up can induce morphological modifications in the receiving water body.

The dynamics of the hyperpycnal plume are dominated by its buoyancy and momentum. Buoyancy is expressed as the depth-averaged relative density difference R_d, and momentum by the Froude number Fr. From the river mouth to the plunge location, R_d and Fr are defined as $R_d = (\rho_d - \rho_a)/\rho_a$ and $\mathrm{Fr} = U/\sqrt{gH}$. Here, U and ρ_d are, respectively, the depth-averaged velocity and density of the hyperpycnal current, H is the local water depth and g is the magnitude of gravitational acceleration. Fr and R_d are often combined in the densimetric Froude number Fr_d (e.g., Akiyama & Stefan, 1984; Sequeiros, 2012),

$$\mathrm{Fr}_d = \frac{\mathrm{Fr}}{R_d} = \left.\frac{U}{\sqrt{gH\left(\rho_d - \rho_a\right)/\rho_a}}\right|_{y/B_0=0} \tag{1}$$

These parameters are calculated at the central plane ($y/B_0 = 0$; B_0 is the width of the river channel at the mouth and y is the distance along the transverse axis in a Cartesian coordinate system, Figure 1a). The subscript "0" denotes initial parameters at the river mouth. Most previous laboratory studies focused on laterally confined receiving waters (Akiyama & Stefan, 1984; Arita & Nakai, 2008; Fleenor, 2001; Lamb et al., 2010; Lee and

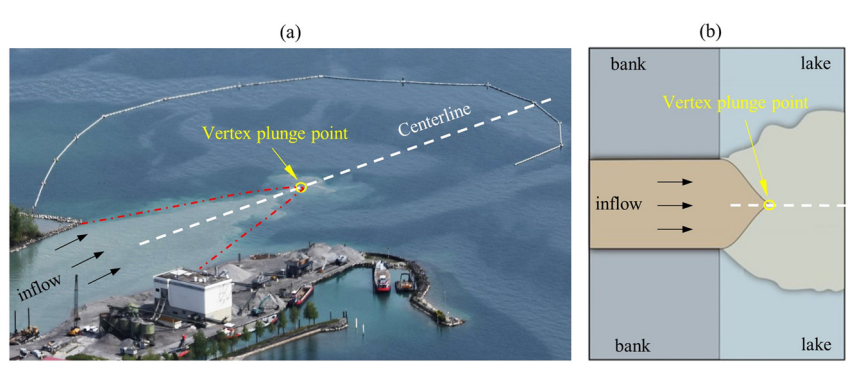

Figure 2. (a) Aerial view of the Rhône River mouth (inflow) in Lake Geneva taken on 1 May 2017 at 16:34 (local time). The mean surface triangular pattern (red-dashed lines) of the unconfined plunging and vertex plunge point was determined from the difference in colors of the turbid sediment-laden river flow and the clear ambient water. The gray circular structure is a floating barrier (about 1 m deep) used to retain driftwood. (b) Plan view sketch of an unconfined plunging river plume.

Yu, 1997; Singh & Shah, 1971, Figure 1), where plunging occurs when Fr_d decreases from Fr_{d-0} at the river mouth to a critical value called the plunging densimetric Froude number, Fr_{d-p} (e.g., Akiyama & Stefan, 1984). Laterally confined configurations may occur in river-dammed reservoirs where the original river bed formed a subaqueous channel and the reservoir is laterally confined by the slowly diverging river valley, for example, the Beznar Reservoir, Spain (Cortés et al., 2014), and Xiaolangdi Reservoir, China (Kostaschuk et al., 2018). For constant-width geometries and no sediment deposition, the variation of Fr_d until the plunge location can be expressed as (Arita & Nakai, 2008)

$$\mathrm{Fr}_d(x) = \mathrm{Fr}_{d-0}\left(\frac{H_0}{H_0 + x\tan\beta}\right)^{3/2} \tag{2}$$

where β is the bottom slope. To determine the plunge location, a layer-averaged thickness $h_c(x)$ that describes the vertical extent of the confined hyperpycnal plume was defined by Lee and Yu (1997):

$$h_c = \left.\frac{\left(\int_{z_b}^{z_o} \overline{u}\,dz\right)^2}{\int_{z_b}^{z_o} \overline{u}^2\,dz}\right|_{y/B_0=0} \tag{3}$$

where z_b represents the depth of the bottom boundary and z_o denotes the depth of the position where $\overline{u}$, the time-averaged longitudinal velocity, decreases to zero. In confined plunging, $h_c(x)$ first increases because of the sloping boundary, then reaches a local maximum. Thereafter, it decreases to a local minimum, before finally again increasing due to the entrainment of ambient water (Lee and Yu, 1997). The location of the local maximum of $h_c(x)$ defines the location of the plunge ($x = x_p$), while its local minimum defines the location where the plunging plume is transformed into an underflow ($x = x_{\mathrm{ud}}$). The plunging densimetric Froude number Fr_{d-p} is calculated from Equation 1 with parameters at the plunge location. Hereinafter, the subscript "p" denotes the parameters at $x = x_p$. In confined plunging, it is often assumed that Fr_{d-p} is a constant with a value close to 0.5, although values in the range 0.4–0.8 have been reported in the literature (Akiyama & Stefan, 1984; Fleenor, 2001; Lamb et al., 2010; Lee & Yu, 1997; Parker & Toniolo, 2007; Singh & Shah, 1971).

Different inlet and boundary conditions inside the plunging hyperpycnal plume cause two different types of flow (Arita & Nakai, 2008; Spigel et al., 2005): (a) the plume attaches to the bottom boundary or (b) the plume separates from the bottom and forms a recirculation zone below it. Based on laboratory experiments, Arita and Nakai (2008) concluded that the latter case occurs when $\mathrm{Fr}_{d-0} > 1.4$ and $\beta > 7°$.

During the plunging process, the hyperpycnal plume entrains ambient waters. As a result, the underflow discharge Q_{ud} at $x = x_{\mathrm{ud}}$ is larger than the inflow discharge. The underflow discharge can be obtained from

$$Q_{\mathrm{ud}} = \int_A \overline{u}\,dA \text{ at } x = x_{\mathrm{ud}} \tag{4}$$

where A represents the cross-sectional area of the hyperpycnal plume defined by a specific density contour (e.g., Tseng and Chou, 2018). The entrainment coefficient, E, describes the amount of ambient water transported across the density interface into the hyperpycnal plume during plunging:

$$E = (Q_{\mathrm{ud}} - Q_0)/Q_0 \tag{5}$$

Laboratory experiments on confined plunging reported values for E in the range 0.02–0.2 (Farrell & Stefan, 1988; Fleenor, 2001; Lamb et al., 2010; Lee & Yu, 1997).

In lakes or oceans, river inflow can develop laterally after leaving the inflow channel (Figure 2); thus, the plunging of a hyperpycnal inflow can be three-dimensional (3D). Examples of unconfined plunging are the Lillooet River entering Lillooet Lake (Canada; Best et al., 2005), the Slims River flowing into Kluane Lake (Canada; Crookshanks & Gilbert, 2008), and the Rhône River plunging into Lake Geneva (Switzerland; Piton et al., 2022; Soulignac et al., 2021). Figure 2a gives an aerial view of the Rhône River mouth showing a triangular pattern on the water surface. A sketch of the unconfined plunging process is shown in Figure 2b. In unconfined plunging, Hogg et al. (2013) defined the plunge location as the place on the surface where the ambient waters from both sides of the progressively plunging plume meet, that is, the vertex of the surface triangle. Hereinafter, this

location is referred to as the vertex plunge point in the unconfined case to distinguish it from the plunge location in confined plunging. Hogg et al. (2013) presented a theoretical approach to predict the shape of the triangle and the vertex plunge point as a function of the inflow parameters for the case of a horizontal bottom.

Thus far, no detailed measurements of the velocity and density fields in the unconfined plunging zone are available in the literature. Yet, such data are needed to quantify the main characteristics of unconfined plunging, that is, the location of the vertex plunge point, plunging densimetric Froude number, and entrainment coefficient and how they are related to control parameters, such as the inflow densimetric Froude number Fr_{d-0} and bottom slope β. Laboratory experiments were conducted by Hauenstein and Dracos (1984) using dye and fine sediments to visualize the spreading of unconfined plunging plumes over a sloping bottom. They proposed an integral model to estimate the lateral spreading and entrainment of the hyperpycnal plume. Johnson, Ellis, et al. (1987), Johnson, Farrell, et al. (1987), Johnson et al. (1989), and Stefan and Johnson (1989) experimentally investigated plunging currents in diverging channels (3–90°) with a horizontal bottom. They observed that the plunging current separates from the sidewalls and becomes laterally unconfined when the diverging angle exceeds 25°, while Fr_{d-p} depends on Fr_{d-0} and the diverging angle. Chen et al. (2013) and Tseng and Chou (2018) showed numerically that the dynamics of the plunging are substantially modified by a sloping bottom. However, their (Reynolds-averaged) models were validated only with laboratory data from confined experiments.

In this paper, results from a unique set of laboratory experiments and numerical modeling of unconfined plunging are presented. These allow for a systematic characterization of this 3D process. The detailed velocity and density fields obtained from the experiments are used to quantify the main characteristics of the plunging plume and to validate the numerical model. The validated model is then applied to investigate an extended range of initial and boundary conditions for additional quantitative analyses (e.g., to determine the role of control parameters). The results for unconfined 3D plunging are also compared with results from laterally confined, two-dimensional (2D) cases. In particular, we focus on the following questions:

1. How do 3D flow patterns in unconfined plunging differ from 2D-confined plunging patterns?
2. How does the flow inside the unconfined plunging hyperpycnal plume develop? Does flow separation occur near the bottom boundary?
3. What are the control parameters of the unconfined plunging process and how do they affect the plunging dynamics?
4. Do characteristics of confined plunging, such as constant Fr_{d-p} and limited entrainment $E < 0.2$, also apply to unconfined plunging?

Figures and text with the prefix S, which provide details and clarifications of topics discussed in the main text, are found in the Supporting Information (SI) section.

2. Materials and Methods

2.1. Control Parameters and Their Investigated Range

The dynamics of unconfined plunging depends on g, B_0, H_0, β, ρ_0, ρ_a, U_0, and the kinematic viscosity υ. According to the Buckingham Π theorem (Garrett, 1960), these can be grouped into independent nondimensional parameters, for example, the aspect ratio H_0/B_0, the bottom slope β, the Reynolds number $\mathrm{Re}_0 = U_0H_0/\upsilon$, the Froude number Fr_0, and the relative density excess R_0. The latter two can be combined into Fr_{d-0} (Equation 1). It is important to determine whether Fr_{d-0} is the only dominant control parameter or if both of its constituents Fr_0 and R_0 must be considered. The range of investigated control parameters in the present laboratory experiments and numerical investigations is summarized in Table 1.

This investigation was motivated by ongoing ECOL field studies of the negatively buoyant Rhône River inflow into Lake Geneva (e.g., Piton et al., 2022; Soulignac et al., 2021). The river channel aspect ratio $H_0/B_0 = 0.04$ and lake bottom slope of $\beta = 8°$ were reproduced in the laboratory experiments. Four experimental cases were investigated with a relative density difference R_0 ranging between 8×10^{-4} and 4×10^{-3}, and with two Froude numbers Fr_0 (0.08 and 0.13), resulting in two sets of Fr_{d-0} values (2 and 3, Cases 1–4, Table 1, A). The corresponding inflow Reynolds numbers in laboratory experiments are inherently several orders of magnitude smaller than those under field conditions. The values of Re_0 between 6,000 and 9,000 are, however, large enough to guarantee turbulent flow conditions.

Table 1
Summary of Parameters Used in Experimental and Numerical Cases

Case	Q_0 (l s^{-1})	$10^3 R_0$	Fr_{d-0}	Fr_0	Re_0	β (°)
A. Experimental and corresponding numerical cases for unconfined plunging						
1	12	1.9	2	0.08	6,000	8
2	18	4.09	2	0.13	9,000	8
3	12	0.8	3	0.08	6,000	8
4	18	1.9	3	0.13	9,000	8
B. Extended numerical cases for unconfined plunging						
5	6	0.45	2	0.04	3,000	8
6	24	7.2	2	0.17	12,000	8
7	6	0.2	3	0.04	3,000	8
8	24	3.2	3	0.17	12,000	8
9	12	0.45	4	0.08	6,000	8
10	12	0.29	5	0.08	6,000	8
11	6	0.05	6	0.04	3,000	8
12	12	0.2	6	0.08	6,000	8
13	18	0.45	6	0.13	9,000	8
14	24	0.8	6	0.17	12,000	8
15	12	1.9	2	0.08	6,000	4
16	12	1.9	2	0.08	6,000	0
C. Numerical cases for confined plunging						
17	12	1.9	2	0.08	6,000	8
18	12	0.8	3	0.08	6,000	8
19	12	0.45	4	0.08	6,000	8
20	12	0.29	5	0.08	6,000	8
21	12	0.2	6	0.08	6,000	8

After the numerical model was validated with the experimental data (Table 1, A), it was applied to expanded ranges of control parameters (Table 1, B) and also a confined configuration (Table 1, C):

1. Fr_{d-0} values from 2 to 6 were investigated based on a variety of combinations of Fr_0 and R_0 values. This range of Fr_{d-0} values is representative of the Rhône River inflow into Lake Geneva. Only cases with $\mathrm{Fr}_{d-0} > 1$ were considered since the plunge is expected to occur inside the inlet channel if $\mathrm{Fr}_{d-0} < 1$ (Johnson, Farrell, et al., 1987; Spigel et al., 2005).
2. The influence of the bottom slope angle β was investigated numerically by also considering a smaller bottom slope ($\beta = 4°$) and a horizontal bottom ($\beta = 0°$).
3. Confined plunging was simulated using the validated numerical model for the same range of Fr_{d-0} (from 2 to 6) for a comparison with unconfined plunging.

2.2. Laboratory Experiments

The laboratory experiments were carried out in the Coriolis Platform, a 13-m diameter by 1.2-m deep circular tank at Laboratoire des Écoulements Géophysiques et Industriels (LEGI), Université Grenoble Alpes, CNRS, Grenoble, France). A sketch of the experimental setup is shown in Figure 3a; more details are given in Text S1 and Figure S1.1 in Supporting Information S1. The Rhône River inflow into Lake Geneva was simulated at a scale of 1:60 by a 2-m wide by 4-m-long straight inflow channel with a rectangular cross-section and horizontal bottom that was positioned 0.67 m above the bottom of the tank. The water depth inside the inlet channel was maintained at $H_0 = 0.08$ m, resulting an aspect ratio $H_0/B_0 = 0.04$. The channel's downstream end was centered with respect to an inclined flat plate ($\beta = 8°$ slope, 8-m wide by 4.75-m long).

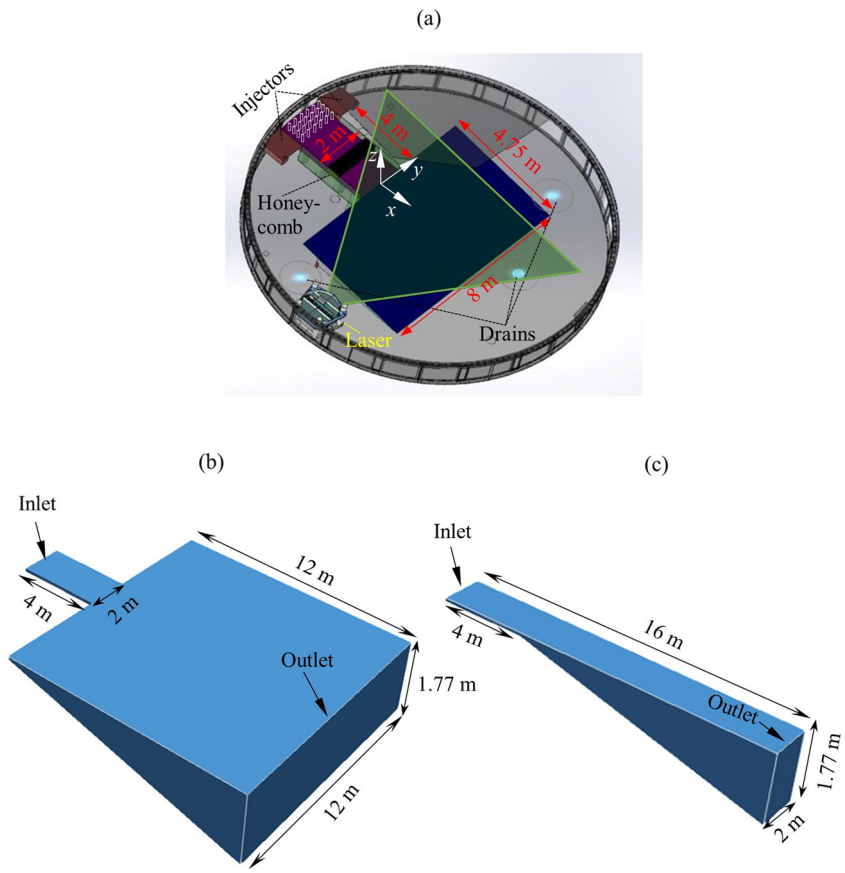

Figure 3. Sketches of the Coriolis Platform (Laboratoire des Écoulements Géophysiques et Industriels, Université Grenoble Alpes) and the numerical domain. (a) The experimental setup consists of injectors, an inlet channel, a sloping bottom plate (inclination 8°), and three drains. The origin of the coordinate system is at the surface of the inlet channel. The large green triangle represents the particle image velocimetry laser sheet. (b) Numerical domain for unconfined plunging composed of an inlet channel with a horizontal bottom and a receiving domain with a sloping bottom. (c) Numerical domain for confined plunging composed of a 4-m-long inlet channel and a 12-m channelized receiving domain.

During the experiments, the tank was first filled with water with density ρ_0. After that, saline water with density ρ_a was fed at the upstream end of the inlet channel via two lateral injectors (Figure 3a). In order to produce a near-uniform velocity distribution across the channel width, a rectangular manifold consisting of an array of full-depth plastic grids (Figure 3a) was installed, followed by a 0.5-m-thick honeycomb placed 1.5-m upstream from the discharge plane. With a constant water discharge Q_0, a stable water flow in the inlet channel was established and verified in preliminary tests (Text S1.1 in Supporting Information S1). A constant water depth in the basin was maintained by extracting water (at rate Q_0) from outlets in the bottom of the tank. These outlets were positioned at the side and below the sloping boundary to minimize perturbations to the hyperpycnal plume. More details of the experimental procedure are given in Text S1 in Supporting Information S1. The Cartesian coordinate system used in this study (x: longitudinal, y: transversal, z: vertical) has its origin (0, 0, 0) on the centerline of the inlet channel at the beginning of the sloping boundary and at the water surface (Figure 3a). The respective time-averaged $(\overline{u}, \overline{v}, \overline{w})$ and transient velocities (u, v, w) are in the (x, y, z) directions. A second Cartesian coordinate system (x_s, $y_s = y$, z_s) with corresponding velocities $(\overline{u}_s, \overline{v}_s = \overline{v}, \overline{w}_s)$ and (u_s, $v_s = v$, w_s) was applied as shown in Figure 1b. For this "s" coordinate system, the longitudinal and vertical coordinates are, respectively, parallel and perpendicular to the bottom slope of the inclined flat plate.

For Cases 1 and 3 (Table 1), flow visualization was realized by injecting fluorescent dye (Rhodamine 6G) at different times during the experiment. A 25-W Yag laser operating at a wavelength of λ = 532 nm was set horizontally and moved vertically (from $z = -0.04$ to -0.29 m) to scan the whole volume of the hyperpycnal plume. Images were captured with GoPro and Nikon D5 cameras.

Particle image velocimetry (PIV) was used for flow visualization and instantaneous velocity determination. The PIV measurements in the plunge region started when this region reached a steady state, which was 3 min after the onset of the experiment. Velocity fields were computed from PIV measurements using a cross-correlation PIV algorithm encoded with the UVMAT software (http://servforge.legi.grenoble-inp.fr/projects/soft-uvmat). For this purpose, an adaptive multi-pass routine was used, starting with an interrogation window of 45×31 pixels and a final window size of 31×21 pixels, with a 70% window overlap. Each element of the resulting vector field represents an area of roughly 0.01×0.01 m. The maximum instantaneous velocity error is estimated to be ~3%. Detailed information about the PIV configuration is provided in Text S1.3 in Supporting Information S1.

2.3. Numerical Model

A numerical model based on the open-source CFD package OpenFOAM (De Lorenzis & Düster, 2020; Jasak, 2009; Weller et al., 1998) was developed to simulate the experimental configurations using a transient solver "*BuoyantBoussinesqPimpleFoam*" for incompressible turbulent flow. The geometry used in the model represents the relevant geometry of the laboratory experiment, consisting of an inlet channel plus a receiving tank with an 8° bottom slope (Figure 3b). The mass and momentum conservation equations are, respectively:

$$\nabla \cdot \langle \mathbf{u} \rangle = 0 \tag{6}$$

$$\frac{\partial \langle \mathbf{u} \rangle}{\partial t} + \nabla \cdot (\langle \mathbf{u} \rangle \otimes \langle \mathbf{u} \rangle) = -\nabla \left(\frac{\langle p \rangle}{\rho_a} \right) + \frac{1}{\rho_a} \nabla \cdot (\tau + \tau_t) + (\langle R \rangle + 1)\, \mathbf{g} \tag{7}$$

where $\langle ... \rangle$ denotes the LES space scale filter, $\mathbf{u}$ the velocity vector, t time, p pressure, $\boldsymbol{\tau}$ the resolved stress tensor, $\boldsymbol{\tau}_t$ the sub-grid scale (SGS) turbulent stress tensor, ρ the local density, $R = (\rho - \rho_a)/\rho_a$ the relative density difference, and $\mathbf{g}$ the gravitational acceleration. The momentum equation is based on the Boussinesq approximation, that is, density variations are considered only in the buoyancy term (e.g., Gray & Giorgini, 1976; Mayeli & Sheard, 2021). Transport of salt was computed using the incompressible mass diffusion equation (Cantero et al., 2007),

$$\frac{\partial R}{\partial t} + \mathbf{u} \cdot \nabla R = \nabla^2 (\alpha_{\text{eff}} R) \tag{8}$$

where $\alpha_{\text{eff}} = \upsilon/\text{Sc} + \upsilon_t/\text{Sc}_t$ is the effective diffusivity with $\text{Sc} = \upsilon/D$ being the Schmidt number and $\text{Sc}_t = \upsilon_t/K$ the turbulent Schmidt number. Here, υ is kinematic viscosity, υ_t is turbulent viscosity, D is molecular diffusivity, and K is eddy diffusivity. Following previous studies on density currents (e.g., Cantero et al., 2007; Härtel et al., 2000; Ooi et al., 2009; Özgökmen et al., 2004), Sc is assumed to be unity, which has almost no effect on the numerical results if $R \ll 1$ (Ooi et al., 2009), since molecular diffusion is negligible. Most previous studies took the turbulent Schmidt number, Sc_t, in the range 0.7–0.9 (Tominaga & Stathopoulos, 2007). Here, $\text{Sc}_t = 0.85$ was applied.

The computational domains for the unconfined and confined geometries are shown in Figure 3. Comparisons of the unconfined and confined plunging were likewise performed with the domain shown in Figure 3c for the latter case. The domain for confined plunging is a 2-m-wide channel with two sections: a 4-m-long inlet with a horizontal bottom and a 12-m-long receiving section with an 8° sloping bottom. Additional details of the numerical model setup (e.g., numerical schemes, treatment of boundary conditions, and grid independence test) are provided in Text S2 in Supporting Information S1.

3. Results and Discussion

3.1. Main Features of Velocity and Density Patterns

In all experimental and numerical cases investigated (Table 1), qualitatively similar results of velocity and density patterns were obtained. In this section, details of the flow field and the density field development will first be shown for Case 3 as a representative example to present the 3D flow patterns of unconfined plunging. Thereafter, results from all cases will be combined to determine the parameters that control the plunging process in Sections 3.2 and 3.3.

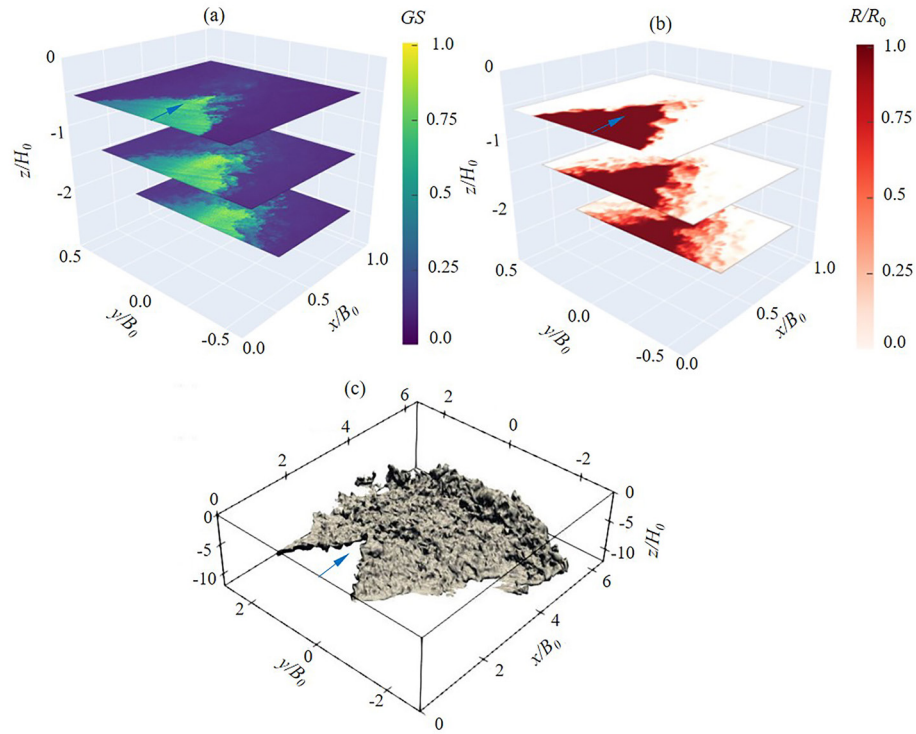

Figure 4. (a) Dye-visualized images of the hyperpycnal plume taken at three different depths in experimental Case 3 (Table 1). (b) Density patterns of the hyperpycnal current on the same three planes calculated from the numerical model. (c) 3D shape of the hyperpycnal current as delineated by an isopycnic surface ($R = 0.2R_0$) in the numerical model. The blue arrows in the plots indicate the inflow direction. In panel (a), the color bar presents the dimensionless gray scales, nondimensionalized by the maximum gray scales of each image. In panel (b), the color bar presents the density ratio R/R_0.

3.1.1. Density Field at Different Vertical Levels

Figure 4a shows the dye-visualized images at three depths in experimental Case 3. For comparison, the density distributions at the same planes calculated from the numerical model are illustrated in Figure 4b. Figures 4a and 4b presents the changes in the structure of the plunge region below the water surface. With increasing depth, the core of the triangular surface pattern gradually decreases due to buoyancy-induced plunging of the inflow and entrainment of ambient water. The numerical model also provides a more detailed 3D shape of the plunge region for a specific isopycnic surface ($R = 0.2R_0$) as shown in Figure 4c. The hyperpycnal plume converges toward the centerline near the water surface after entering the ambient waters (Figure 4). It forms a triangle at the surface, but spreads laterally close to the bottom (Figure 4c). This behavior is markedly different from confined plunging.

3.1.2. Comparison of Measured and Modeled Mean Velocity Fields

Figures 5a–5c presents the time-averaged (over 50 s) velocity distributions on different planes for Case 3. The location of the vertex plunge point (x_p) and the location where the plunging plume transforms into an underflow (x_{ud}) are discussed in more detail in Section 3.2. Since the inlet flow and the plunging process can be assumed to be symmetrical (Hauenstein, 1982; Hauenstein & Dracos, 1984), the symmetry of each panel in Figure 5 illustrates the good agreement between the numerical model results and the experimental data. The distribution of longitudinal velocities at $z = -0.5H_0$ is also triangular (Figure 5a). The boundary of the triangle extracted from the dye-visualized images (uppermost layer in Figure 4a) is plotted for comparison (red stars; for details refer to Text S3 in Supporting Information S1). In the deeper section at $z = -2H_0$ (Figure 5b), a larger triangle is identified. Inside this triangle, a region with reduced velocity (low-velocity region) exists, marked by the brown-dashed lines. Close to the bottom (Figure 5c), this low-velocity region is still evident in the plunging region ($0 < x \leq x_{ud}$). In the underflow region after plunging ($x \geq x_{ud}$) (Figure 5c), the largest longitudinal velocities are located at the centerline ($y/B_0 = 0$) and the current spreads laterally outward on both sides.

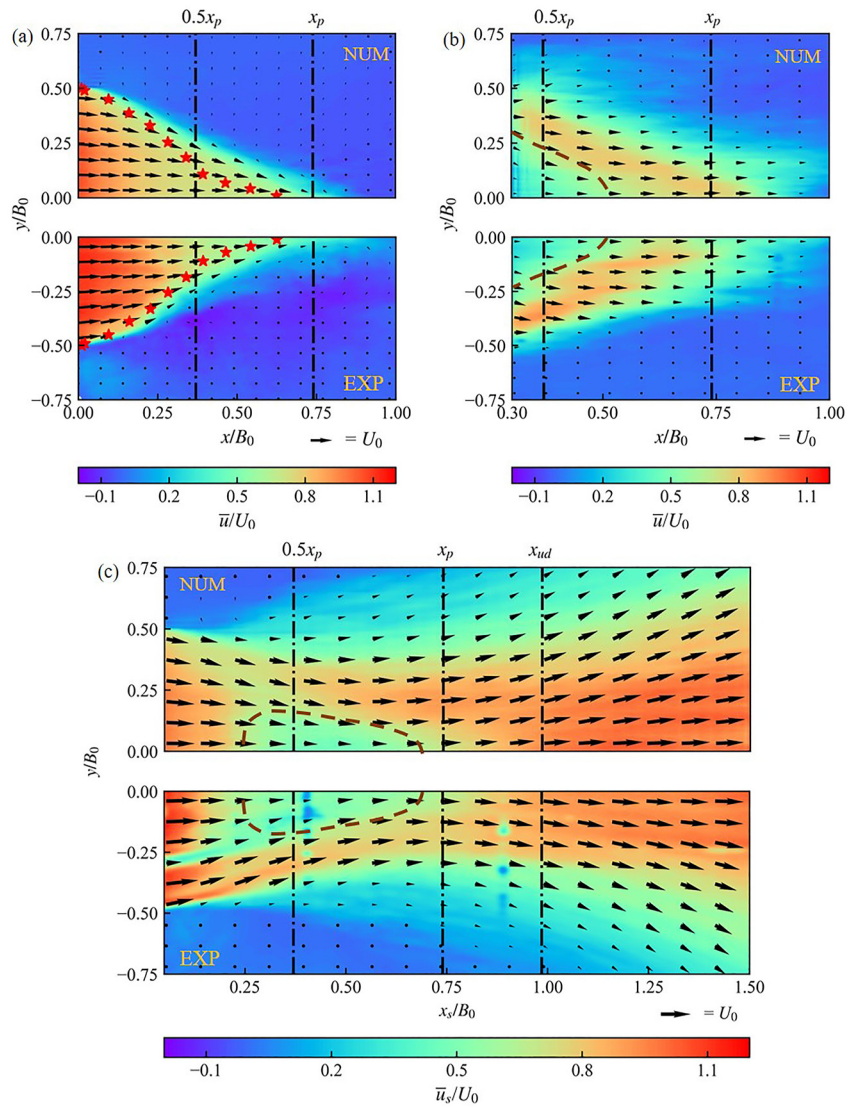

Figure 5. Longitudinal (time-averaged) velocity distribution for Case 3 in the: (a) first plane ($z = -0.5H_0$, plane *a-a* in Figure 1b), (b) deeper plane ($z = -2H_0$, plane *b-b* in Figure 1b), and (c) near-bottom-inclined plane parallel to the slope (0.04 m above the bed, plane *c-c* in Figure 1b). The red stars in panel (a) indicate the triangular pattern obtained from dye-visualized images (for details, see Text S3 in Supporting Information S1). The low-velocity region inside the plunging current is marked by the brown dashed lines in panels (b and c). The black dashed-dotted vertical lines present the locations of $x = 0.5x_p$ inside the plunge region, $x = x_p$ at the vertex plunge point, and $x = x_{ud}$ where the plunging plume transforms into an underflow. The top half of each panel presents numerical modeling results, and the bottom half, experimental results. Black arrows give the mean flow direction and color bars, the range of velocity. The resolution of this figure is 0.01 × 0.01 m.

Figures 6a and 6b compare the velocity along the centerline on the plane *a-a* ($z = -0.5H_0$) and 0.04 m above the sloping bottom on plane *c-c*. On plane *a-a*, the horizontal velocity decreases with distance from the end of the inlet channel due to loss of momentum and eventually reaches zero. Near the bottom, the centerline current velocity parallel to the bottom slope first decreases rapidly and then increases again, indicating the zone with reduced velocity inside the plunging plume, marked by brown-dashed lines in Figure 5c. In the underflow region ($x \geq x_{ud}$), the longitudinal velocity $\overline{u}_s$ near the bottom at the centerline tends toward a constant value (Figures 5c and 6b) due to the combined effect of acceleration ($Rg\sin\beta$) and entrainment.

Transversal profiles of the longitudinal, transversal, and vertical velocity components at $x = 0.5x_p$ and $z = -0.5H_0$ are plotted in Figure 6c. In this panel, the longitudinal velocity has a nearly constant value inside the triangular region and decreases quickly outside it. On each side, the transversal velocity points inward toward the centerline

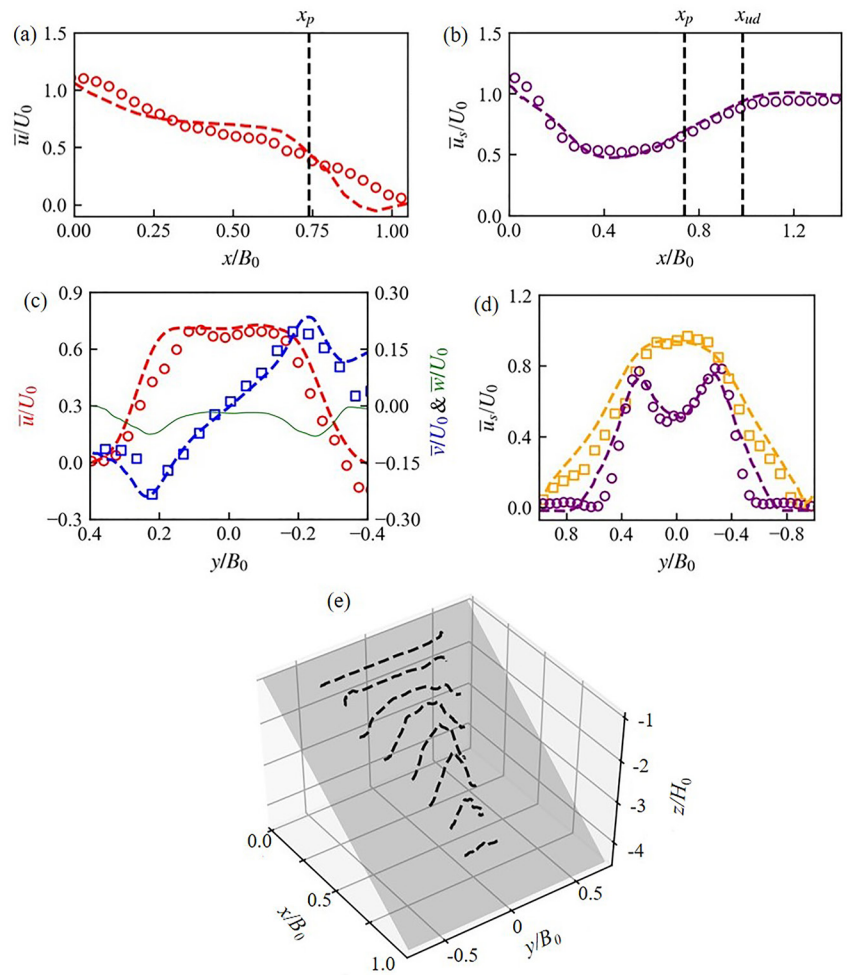

Figure 6. Comparison of numerical results (lines) and experimental results (circles and squares) for Case 3: (a) Centerline longitudinal velocity at $z = -0.5H_0$. (b) Centerline velocity parallel to and 0.04 m above the sloping bottom. The locations of the vertex plunge point (x_p) and where the plunging plume transforms into an underflow (x_{ud}) are marked by the black dashed lines. (c) Transversal profiles of velocities at ($x/x_p = 0.5$; $z/H_0 = -0.5$). Red and blue present the longitudinal and transversal velocities, respectively. For the vertical velocity, only numerical data are available (green line). (d) Transversal profiles of experimental and numerical $\overline{u}_s$ at 0.04 m above the bottom (plane *c-c*, Figure 1) inside the plunge region at $x = 0.5x_p$ (purple) and in the underflow region at $x = x_{ud}$ (orange). (e) 3D shape of the low-velocity zone defined by the iso-surface of $\overline{u} = 0.6U_0$ based on the numerical results. Note that the axes have different ranges in the panels.

with maximum (positive) and minimum (negative) values located near the edge of the surface triangle. This inward transversal velocity results from the transverse lock-exchange-type flow generated by the lateral pressure gradient between the hyperpycnal plume and ambient water as discussed in Hogg et al. (2013) and Tseng and Chou (2018). The superposition of the longitudinal and inward transversal velocity components results in a velocity direction that follows the edge of the surface velocity triangle at the interface (Figure 5a). The vertical velocity (green line, Figure 6c), obtained from the numerical model, is directed downward in the whole transect with two peaks near the edges of the surface triangle. Figure 6d presents the near-bottom downslope velocity profiles (plane *c-c*) at $x = 0.5x_p$ and $x = x_{ud}$. At $x = 0.5x_p$, inside the plunging region (purple), two local velocity maxima delimit a lower velocity region near the centerline. Again, this behavior is due to the low-velocity zone observed in Figures 5b and 5c. At $x = x_{ud}$ (orange), however, the current is an underflow and the velocity profile only has one maximum at the centerline. The 3D shape of the low-velocity zone can be visualized by the iso-surface of $\overline{u} = 0.6U_0$ in Figure 6e (numerical results).

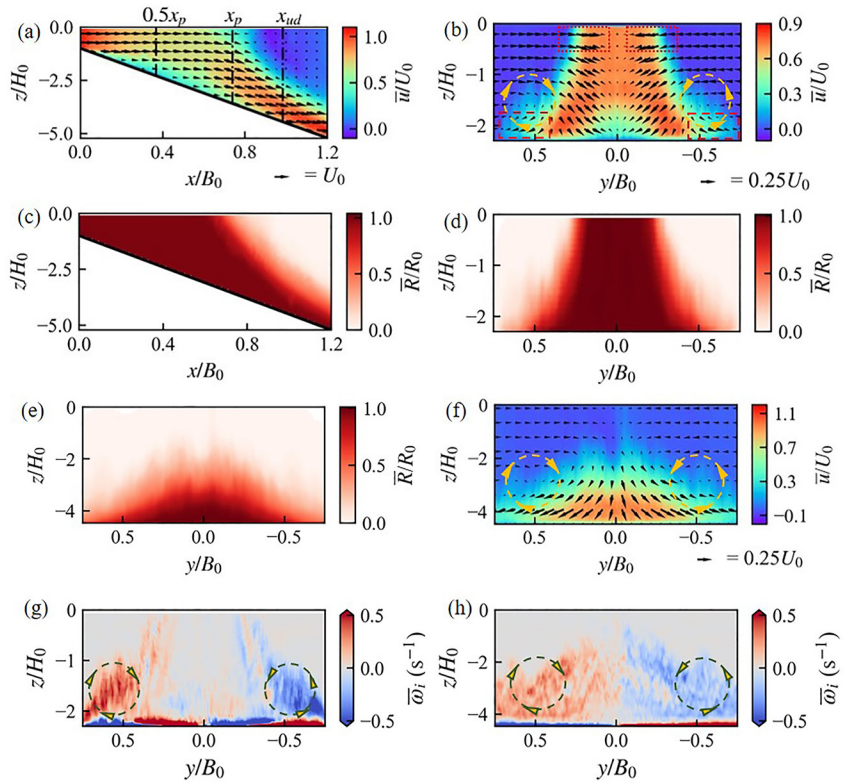

Figure 7. Numerically determined velocity and density fields for Case 3. (a) Velocity and (c) density fields in the central plane $y/B_0 = 0$. The three black dashed-dotted lines mark the locations where $x = 0.5x_p$, $x = x_p$, and $x = x_{ud}$. (b) Velocity and (d) density fields in the cross section at $x = 0.5x_p$. (e) Density and (f) velocity fields in the cross section at $x = x_{ud}$. (g) Vorticity in the cross section at $x = 0.5x_p$ and (h) vorticity at $x = x_{ud}$. Circles in panels (b) and (f–h) show suggested secondary circulations.

3.1.3. Modeled Mean Velocity Fields in the Central Plane and Cross Sections

Model results for the velocity distribution clearly show a low-velocity zone around the centerline (Figures 7a and 7b). However, the time-averaged relative density field ($\overline{R}$) in the corresponding sections indicates that the density in this low-velocity zone is uniform ($= R_0$; Figures 7c and 7d). The low-velocity zone is created by flow separation that occurs when the slope changes at the junction of the inlet channel and the sloping bed of the receiving waters. Blanckaert (2015) divided the flow separation process into two stages: In the first stage, the velocity profile develops a deficit but remains oriented downward, followed by the second stage where flow reversal occurs near the boundary and a recirculation zone develops. Only the first-stage separation occurs in the cases considered here. The density distribution remains uniform within the plunging flow, whereas it is diluted due to entrainment of ambient water across the interface (Figures 7c and 7d). Figure 7b presents the transverse and vertical velocities at $x = 0.5x_p$. Near the bottom, the density difference between the hyperpycnal plume and ambient water causes a lateral pressure gradient. This results in an outward transversal flow on both sides near the bottom (red dashed-lined boxes). As a consequence, similar to lock-exchange flow (e.g., Shin et al., 2004), an inward transversal flow toward the centerline is generated near the surface (red dotted-lined boxes) to keep the mass balance. Interestingly, transverse velocities converging toward the center of the plunging flow are also observed in the region $-0.3 < y/B_0 < 0.3$ near the bottom as already reported in the numerical study of Tseng and Chou (2018) and confirmed by our experimental data in Figure 5c. In the area $0.25 < x/B_0 < 0.5$, $-0.3 < y/B_0 < -0.1$, the quiver plot shows transverse velocities directed toward the centerline. These near-bottom converging velocities occur due to the much higher downward velocity at the two sides ($y/B_0 \approx \pm 0.3$) compared with the centerline.

After plunging, the hyperpycnal plume flows down the slope in the underflow region. Figures 7e and 7f present the density and velocity fields at $x = x_{ud}$. Most of the dense fluids are found in a thin layer at the bottom (Figure 7e). In

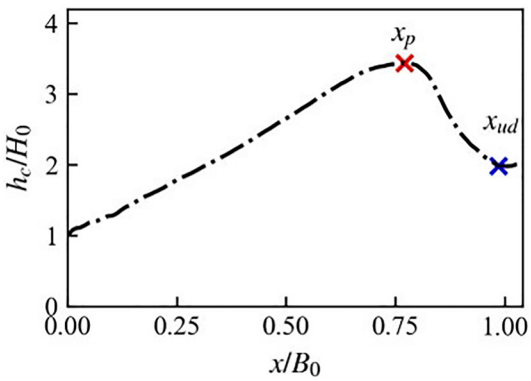

Figure 8. Modeled variations of layer-averaged hyperpycnal current thickness in the central section of Case 3. The red cross indicates the vertex plunge point (x_p) and the blue cross marks the location where the plunging plume transforms into an underflow (x_{ud}).

contrast to the plunging region (Figure 7d), only downward-outward secondary velocities were observed inside the hyperpycnal plume (Figure 7f), which explains the lateral spreading of the underflow (Figure 5c).

In both cross sections, at $x = 0.5x_p$ and $x = x_{ud}$, secondary circulations at the dense/ambient flow interfaces are observed, highlighted by the circles in Figures 7b and 7f (clockwise on the left side and counterclockwise on the right). Figures 7g and 7h present the time-averaged vorticity field, $\overline{\omega}_i = \partial\overline{w}/\partial y - \partial\overline{v}/\partial z$, in these two sections. High values on both sides of the hyperpycnal plume indicate rotating secondary circulations.

3.2. Determination of Parameters x_p, x_{ud}, Fr_{d-p}, and E

Although the location of the vertex plunge point can be estimated from specific contours of velocity and/or density at the surface, the results will depend on the threshold value used in the definition. In confined plunging, Lee and Yu (1997) suggested that x_p and x_{ud} can be determined from variation of the layer-averaged thickness of the hyperpycnal plume $h_c(x)$ along the central plane ($y/B_0 = 0$) (details in Section 1). In the present study, this method is also applied to the numerical unconfined cases. Figure 8 illustrates the variation of $h_c(x)$ in the unconfined numerical Case 3. The local maximum of $h_c(x)$ gives the value of x_p, while the local minimum gives the location where the plunging plume transforms into an underflow (x_{ud}). After x_p and x_{ud} are determined, the plunging densimetric Froude number is calculated using Equation 1 and the entrainment coefficient is obtained by Equations 4 and 5 using $\overline{R} = 0.2R_0$ to determine the cross-sectional area A.

3.3. Parameters Dominating the Plunging Process

Since the results obtained for all cases were similar to those of Case 3 discussed above, they were combined in order to determine their dependence on Fr_0, R_0, Fr_{d-0}, β, and the lateral confinement, which are assumed to be the main controls.

3.3.1. Influence of Fr_0, R_0, and Fr_{d-0}

Figure 9a shows half of the modeled density contour ($\overline{R} = 0.95R_0$) at $z = -0.5H_0$, for cases with different values of Fr_{d-0}, Fr_0, and R_0 (Table 1). Experimental data from the dye-visualized images are also depicted in this figure for comparison (gray scales of the dye images are approximately linked to the density; see Text S3 in Supporting Information S1 for details). Figure 9b presents half of the velocity contour ($\overline{u} = 0.3U_0$) at $z = -0.5H_0$ in the

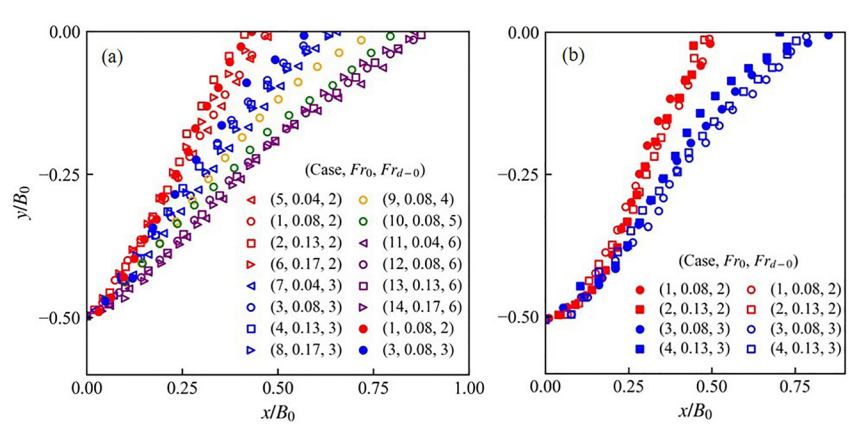

Figure 9. (a) Points on the density contours $\left(\overline{R} = 0.95R_0\right)$ at $z = -0.5H_0$ for Cases 1–14 (Table 1). (b) Points on the velocity contours $\left(\overline{u} = 0.3U_0\right)$ at $z = -0.5H_0$ for Cases 1–4. In both panels, each case is identified by Case, Fr_0, and Fr_{d-0} values in the legend (corresponding R_0 values are given in Table 1). Open and filled symbols present the numerical and experimental data, respectively. Symbols indicate cases with different Fr_0, and colors give cases with different Fr_{d-0}.

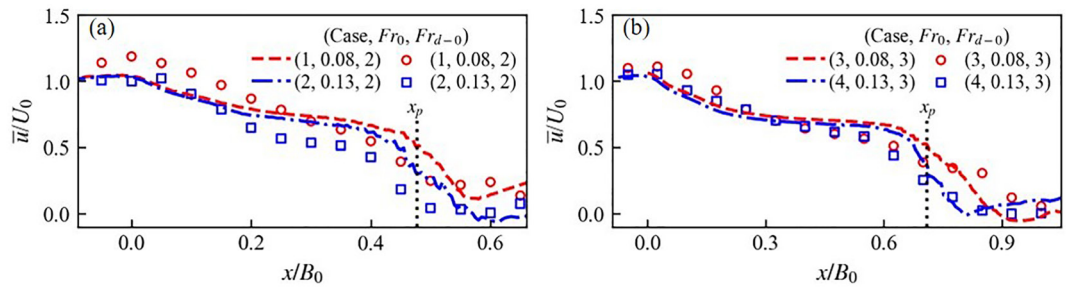

Figure 10. Measured and modeled centerline longitudinal velocity at $z = -0.5H_0$ for (a) Cases 1 and 2 and (b) Cases 3 and 4 (identified by Case, Fr_0, and Fr_{d-0} values in the legend, Table 1). Symbols represent experimental data, while lines are numerical results. The vertical dotted lines locate the vertex plunge point (x_p) obtained numerically. Note that the x/B_0 axes have different ranges.

experiments compared with the corresponding numerical cases. It is evident that the size of the triangle strongly depends on Fr_{d-0}. As Fr_{d-0} increases, the vertex plunge point moves further away from the river mouth, resulting in a larger x_p.

Although different combinations of Fr_0 and R_0 can result in the same Fr_{d-0}, the size of the surface triangle does not change (Figure 9) for given values of Fr_{d-0}. Figure 10 presents the measured and modeled centerline longitudinal velocity at $z = -0.5H_0$ for Cases 1–4. Similar to the surface triangle size, the variation of this centerline velocity is again dependent only on Fr_{d-0} rather than Fr_0 and R_0. Furthermore, the length of the low-velocity zone inside the plunging plume also increases with Fr_{d-0} (Figure 11).

3.3.2. Influence of the Bottom Slope

Figure 12 presents the modeled surface density contour $\left(\overline{R} = 0.95R_0\right)$ for three numerical cases with the same inlet condition ($\mathrm{Fr}_0 = 0.08$, $\mathrm{Fr}_{d-0} = 2$), but with different bottom slopes (β). Investigated bottom slopes include a horizontal bottom, a bottom slope of 4°, and the experimentally investigated bottom slope of 8°. A large difference between the surface triangles is apparent in Figure 12, which shows that the unconfined hyperpycnal plume plunges closer to the river mouth when the bottom boundary slope is larger, as was previously observed by Tseng and Chou (2018). A similar result was reported in confined cases (Arita & Nakai, 2008). The results of the numerical simulation of the horizontal case were compared with the analytical prediction of the surface triangle by Hogg et al. (2013):

$$y = \pm\left(\frac{B_0}{2} - \frac{x\sqrt{g_0' H_0}}{2\overline{u}_{\mathrm{os}}}\right) \tag{9}$$

where $\overline{u}_{\mathrm{os}}$ denotes the inlet velocity at the surface. The numerical results of this study agree well with their model (Figure 12). Equation 9 is based on the assumptions that the centerline velocity on the water surface remains almost constant up to the vertex plunge point and that the lateral converging velocity of the surface triangle follows the law obtained from lock-exchange density currents: $\overline{v}_e = \sqrt{g_0' H_0}/2$. Both of these assumptions are invalid if the bottom boundary is inclined. A comparable analytical solution to Equation 9 for a nonzero bottom slope is not available.

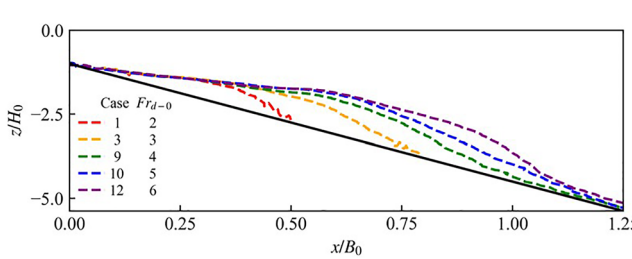

Figure 11. Variation of the length of the low-velocity zone in the central plane, defined by the contour $\overline{u} = 0.6U_0$, in unconfined plunging for numerical cases with $\mathrm{Fr}_0 = 0.08$.

3.3.3. Influence of Lateral Confinement

Figure 13a presents the variation of Fr_d in confined numerical cases with an 8° bottom slope and $\mathrm{Fr}_0 = 0.08$. Fr_d is calculated based on the velocity and density data in the central plane (Equation 1). In the longitudinal direction, Fr_d decreases due to the bottom slope following Equation 2 as suggested by Arita and Nakai (2008). The numerical simulations indicate that the plunge occurs when Fr_d decreases to a critical value close to 0.5, which is consistent with the value obtained by Lamb et al. (2010) using the theoretical model of Parker and Toniolo (2007). When Fr_{d-0} increases, the plunge occurs further away from the river mouth. The decrease of Fr_d is slower in unconfined

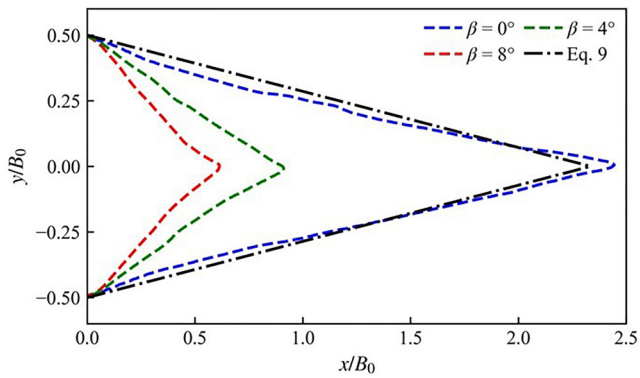

Figure 12. Surface density contours $\left(\overline{R} = 0.95R_0\right)$ for the numerical cases with the same $\mathrm{Fr}_0 = 0.08$ and $\mathrm{Fr}_{d-0} = 2$, but with different bottom slopes (i.e., 0°, 4°, and 8° for Cases 16, 15, and 1 (Table 1), respectively, as indicated by the colors in the legend). The black dashed-dotted lines are the prediction of Equation 9 for the horizontal bottom Case 16.

plunging than in confined plunging (Figures 13a and 13b), implying that Equation 2 is not valid in unconfined cases. Equation 2 is based on the assumption that the discharge per unit width in the central plane (q_c) remains constant before the plunge location, that is, $U_0H_0 = U_c(x)H(x)$. This is valid in confined plunging, for example, in Case 21, where q_c/q_{c-0} remains nearly constant at around unity (Figure 13c, black circles). However, in unconfined plunging, q_c increases longitudinally since the transversal secondary velocity is directed toward the centerline as shown in Figure 7b. The increase of q_c slows down the decrease of Fr_d. As a result, Fr_d at the location where the confined hyperpycnal plume plunges is still greater than 0.5 in the corresponding unconfined case (same value of Fr_{d-0}, compare Figures 13a and 13b). Thereafter, Fr_d continues to decrease in the unconfined case. At the vertex plunge point, Fr_{d-p} in the unconfined cases is still substantially greater than the critical value of ~0.5 that is characteristic of confined plunging. Moreover, Fr_{d-p} is found to increase with Fr_{d-0} and can be larger than unity. These results indicate that the unconfined plunge is not only controlled by a critical value of Fr_{d-p}, but also by the three-dimensional flow patterns inside the plunge region. Indeed, the plunge occurs where the two sides of the hyperpycnal plume meet at the centerline on the surface even though Fr_d is still greater than the critical value for confined cases.

Figure 14a presents the increase of discharge in the plunge region (from $x = 0$ to $x = x_{\mathrm{ud}}$) due to entrainment in four unconfined numerical cases with the same $\mathrm{Fr}_{d-0} = 3$, but different combinations of Fr_0 and R_0. For the cases considered, Fr_0 and R_0 have no influence on the entrainment since Fr_{d-0} does not change. Figure 14b shows the variation of the entrainment coefficient E with Fr_{d-0} in confined and unconfined numerical cases with $\mathrm{Fr}_0 = 0.08$. In confined plunging, E values are found within a narrow range (0.05–0.15), which are similar to results reported in previous experimental studies ranging from 0.02 to 0.2 (Farrell & Stefan, 1988; Fleenor, 2001; Lamb et al., 2010; Lee & Yu, 1997). In unconfined plunging, however, E values are not only significantly larger, but also increase with increasing Fr_{d-0} from 0.4 to 0.7 (Figure 14b). The increase of E with Fr_{d-0} in unconfined cases can be explained by the downstream shift of the vertex plunge point with increasing Fr_{d-0}. This results in a larger interface area along which the entrainment between the riverine inflow and the ambient water occurs.

3.4. Generalization of Results

Field measurements of unconfined temperature-induced plunging were made in the Canale Italsider mouth (Lake Iseo, Italy) by Hogg et al. (2013) and in the Tokaanu Tailrace mouth (Lake Taupo, New Zealand) by Spigel et al. (2005). The related geometry and inlet conditions are listed in Table 2. Numerical simulations for Lake Iseo and Lake Taupo were performed using simplified geometries similar to Figure 3b based on geometric (1:20 scale) and Froude similarity (Table 2). The numerical model predicts $x_p/B_0 = 0.8$ for the Canale Italsider mouth, consistent with the range of 0.6–1.0 reported by Hogg et al. (2013). Hogg et al. (2013) applied Equation 9 to estimate the vertex plunge point $\left(x_{\mathrm{up}} = \overline{u}_{\mathrm{os}}B_0/\sqrt{g_0'H_0}\right.$; they further assumed that $\overline{u}_{\mathrm{os}} = U_0$), resulting in $x_p/B_0 = 2.4$, which is more than double the measured value. This overestimation of x_p is due to the simplifying assumption that the lake bottom is horizontal. For the Tokaanu Tailrace mouth, the numerical model gave $x_p/B_0 = 1.0$, which agrees with the range ($x_p/B_0 = 0.8$–1.0) reported by Spigel et al. (2005). They calculated an entrainment coefficient $E = 1.9$, which is about double the value ($E = 1.1$) determined numerically using Equation 4 to calculate Q_{ud}. This difference is due to the different methods used to obtain Q_{ud}. Spigel et al. (2005) assumed that Q_{ud} = discharge per unit width in the central plane × plume width, which overestimates Q_{ud} since the velocity in the central plane of the underflow region is considerably higher than on the two sides as shown in Figure 5c. If their method is applied to the numerical data, $E = 1.7$ is obtained that is quite close to the value ($E = 1.9$) they reported.

The inflow of the Rhône River (Lake Geneva) is sediment-laden and both the suspended sediment and temperature contribute to the excess density of the hyperpycnal plume. Figure 2a shows the surface triangle at the Rhône River mouth. This image was taken on a day when $\mathrm{Fr}_{d-0} \approx 3.2$ and gives an estimation of the vertex plunge point as $x_p/B_0 \approx 1.0$. The numerical and experimental Case 3 have an Fr_{d-0} value close to this and further that $x_p/B_0 = 0.75$. The underestimation of x_p may result from sediment deposition that is not included in the experiments

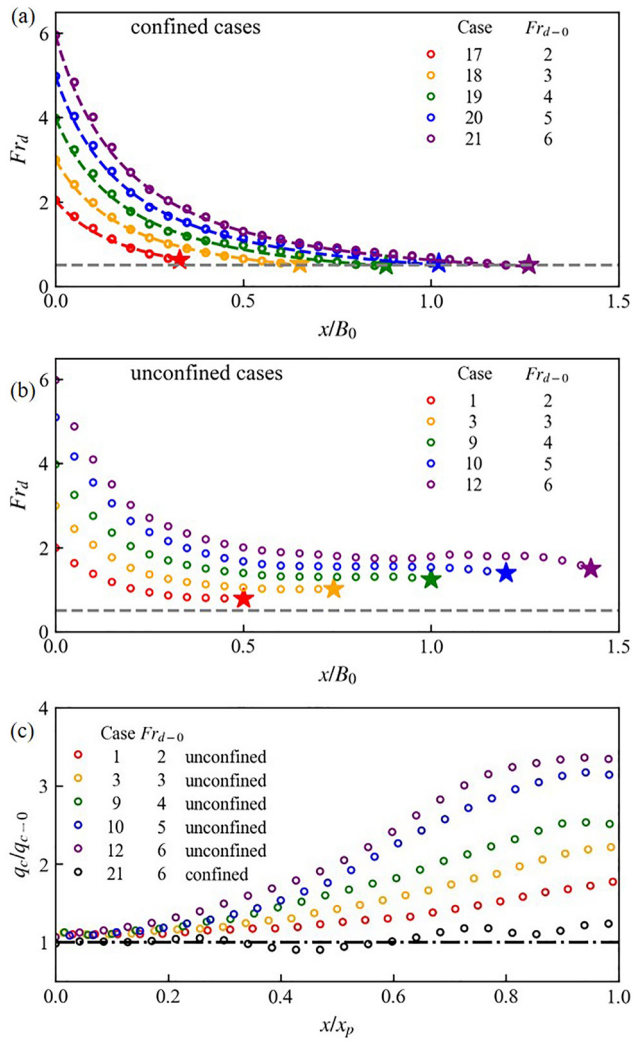

Figure 13. Variation of Fr_d in the central plane from the river mouth to the plunge location (or the vertex plunge point) in the (a) confined and (b) unconfined numerical cases with $Fr_0 = 0.08$. The end point (star) of each curve marks x_p (Figure 1). (c) Modeled variations of discharge per unit width q_c in the central plane of the unconfined cases with $Fr_0 = 0.08$. Modeled variations of q_c in the confined case with $Fr_{d-0} = 6$ and $Fr_0 = 0.08$ (black circles, Case 21, Table 1) are also included and compared with the theoretical result $q_c(x) = q_{c-0}$ (black dashed-dotted line).

or the numerical model. As the hyperpycnal plume develops, it loses momentum, which leads to the deposition of larger-sized suspended sediment, reducing the relative density difference (Piton et al., 2022). Sedimentation may also reduce the bottom slope angle. Both of these mechanisms can lead to a larger x_p in hyperpycnal plunging.

4. Summary and Conclusions

By combining detailed laboratory measurements of the velocity fields and 3D numerical modeling, this study allowed the first characterization of 3D unconfined plunging of a hyperpycnal river plume over a sloping bed and its lateral spreading. The numerical modeling was based on a computational fluid dynamics (CFD) model, which was validated with the experimental results, thus demonstrating that the model is suitable for realistically simulating the unconfined plunging process.

The results of this study reveal that the 3D unconfined plunging process is different from confined (essentially 2D) plunging. In the unconfined plunging process, 3D flow structures are observed: As the hyperpycnal plume is advected longitudinally, currents in the cross sections are directed downward and form transversal lock-exchange type flows on each side of the plunge. This causes the current to converge toward the centerline on the surface creating a triangular shape of velocity/density fields, while spreading laterally near the bottom. The near-bottom lateral spreading further generates secondary circulations on both sides of the hyperpycnal plume.

Inside the unconfined plunging plume, a low-velocity zone exists due to flow separation induced by the transition from the horizontal bottom of the inflow channel to the sloping bed of the receiving waters.

Similar to confined plunging, the inflow densimetric Froude number Fr_{d-0} and the bottom slope β in the receiving water body are the dominant control parameters in unconfined plunging. The same value of Fr_{d-0} can be obtained from different combinations of its constituents Fr_0 and R_0. The results show that plunging characteristics only depend on Fr_{d-0} irrespective of Fr_0 and R_0. Decreasing Fr_{d-0} or increasing the bottom slope causes plunging to occur closer to the river mouth.

In confined plunging, the plunge occurs when the densimetric Froude number Fr_{d-0} decreases to a critical value close to 0.5 and the amount of ambient water entrained into the hyperpycnal plume is quite limited. In unconfined plunging, however, the vertex plunge point is where the two sides of the hyperpycnal plume meet at the centerline on the surface even if Fr_d is still larger than the critical value of unconfined plunging. Since ambient waters can be entrained from both sides into the hyperpycnal current, the entrainment coefficient E in unconfined plunging is found to be much larger than in confined plunging.

This study has made evident the following similarities and differences between confined and unconfined plunging:

Similarities:

1. From the river mouth, the layer-averaged thickness h_c of the hyperpycnal current in the central section first increases and then decreases rapidly after the initiation of plunging, followed by another increase due to entrainment. The variations of h_c can be applied to determine x_p and x_{ud}.
2. The distance from the river mouth to the plunge location (or the vertex plunge point) increases with increasing Fr_{d-0} and decreasing bottom slope β.

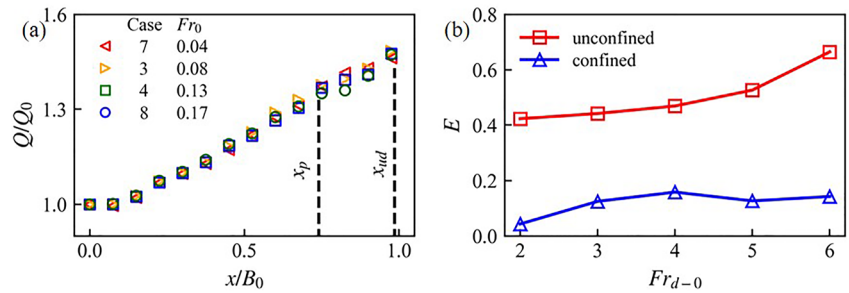

Figure 14. (a) Variations of the normalized discharge Q/Q_0 in four unconfined numerical cases with $\mathrm{Fr}_{d-0} = 3$ but different combinations of Fr_0 and R_0. The black dashed lines give the vertex plunge point and the location where the plunging plume has transformed into an underflow. (b) Comparison of the entrainment coefficient E between the confined (blue, Cases 17–21, Table 1) and unconfined (red, Cases 1, 3, 9, 10, and 12) numerical cases with the same $\mathrm{Fr}_0 = 0.08$.

Differences:

1. Unconfined (3D) plunging flow patterns are different from those of confined (2D) cases.
2. The discharge per unit width at the central section q_c increases longitudinally in unconfined plunging but is constant in confined cases.
3. In confined plunging, the plunge occurs when Fr_d decreases to the critical value (i.e., $\mathrm{Fr}_{d-p} \approx 0.5$). In unconfined cases, however, the vertex plunge point is located where the two sides of the hyperpycnal plume meet at the centerline on the surface.
4. In unconfined plunging, much more entrainment takes place resulting in significantly larger entrainment coefficient E values than in confined cases.

The numerical model results agreed well with previous field observations of unconfined plunging flow. This unique combination of laboratory experiments, numerical modeling, and previous field observations improves the understanding and the characterization of unconfined hyperpycnal river plunging dynamics.

Unconfined hyperpycnal river plume plunging is often observed in lakes. Taking into consideration unconfined plunging processes allows for better understanding of how plunging inflows transport materials and how they mix with ambient waters, and as a result, how they affect water quality, local ecosystems, and morphological evolution. Therefore, the results of the present study can contribute to the development of effective lake management concepts. These findings can also be expected to be applicable to other water bodies where unconfined hyperpycnal river-plume plunging occurs.

Table 2
Comparison Between the Numerical Model and Field Measurements

	U_0 (m s^{-1})	H_0 (m)	B_0 (m)	ρ_a (kg m^{-3})	ρ_0 (kg m^{-3})	β (°)	x_p/B_0	Fr_{d-0}	E	Scale
Canale Italsider mouth (Hogg et al., 2013)										
Field	0.48	1.7	49	997.3	999.4	4.6	0.6–1.0	2.6	–	20
NUM	0.107	0.085	2.45	997.3	999.4	4.6	0.8	2.6	0.5	
Tokaanu Tailrace mouth (Spigel et al., 2005)										
Field	0.63	1.42	96	999.56	999.98	5.5	0.8–1.0	8.2	1.9[a]	20
NUM	0.141	0.071	4.8	999.56	999.98	5.5	1.0	8.2	1.1 (1.7[a])	
Rhône River mouth										
Field	0.14	4.8	120	999.76	999.80	8	1.0	3.2	–	60

[a]Entrainment coefficient using the method in Spigel et al. (2005) to estimate Q_{ud}.

Data Availability Statement

Data reported in this paper and the original image of the Rhône River mouth (Figure 2a) can be downloaded from https://doi.org/10.5281/zenodo.6940788 or https://gitlab.epfl.ch/hashi/wrrdata.git. The Supporting Information file contains more detailed information of the experiments and numerical modeling.

Acknowledgments
The authors are indebted to S. Viboud and T. Valran for their support in conducting the experiments at the Coriolis Platform (Université Grenoble Alpes, CNRS, Grenoble, France) and are grateful to E. J. Hopfinger for fruitful discussions and suggestions.

References

Akiyama, J., & Stefan, H. G. (1984). Plunging flow into a reservoir: Theory. *Journal of Hydraulic Engineering*, *110*(4), 484–499. https://doi.org/10.1061/(ASCE)0733-9429(1984)110:4(484)

Arita, M., & Nakai, M. (2008). Plunging conditions of two-dimensional negative buoyant surface jets released on a sloping bottom. *Journal of Hydraulic Research*, *46*(3), 301–306. https://doi.org/10.3826/jhr.2008.2714

Best, J. L., Kostaschuk, R. A., Peakall, J., Villard, P. V., & Franklin, M. (2005). Whole flow field dynamics and velocity pulsing within natural sediment-laden underflows. *Geology*, *33*(10), 765. https://doi.org/10.1130/G21516.1

Blanckaert, K. (2015). Flow separation at convex banks in open channels. *Journal of Fluid Mechanics*, *779*, 432–467. https://doi.org/10.1017/jfm.2015.397

Branch, R. A., Horner-Devine, A. R., Kumar, N., & Poggioli, A. R. (2020). River plume liftoff dynamics and surface expressions. *Water Resources Research*, *56*(7), e2019WR026475. https://doi.org/10.1029/2019WR026475

Cantero, M. I., Balachandar, S., & Garcia, M. H. (2007). High-resolution simulations of cylindrical density currents. *Journal of Fluid Mechanics*, *590*, 437–469. https://doi.org/10.1017/S0022112007008166

Chen, S. N., Geyer, W. R., & Hsu, T. J. (2013). A numerical investigation of the dynamics and structure of hyperpycnal river plumes on sloping continental shelves: Dynamics of hyperpycnal river plumes. *Journal of Geophysical Research: Oceans*, *118*(5), 2702–2718. https://doi.org/10.1002/jgrc.20209

Cortés, A., Fleenor, W. E., Wells, M. G., de Vicente, I., & Rueda, F. J. (2014). Pathways of river water to the surface layers of stratified reservoirs. *Limnology and Oceanography*, *59*(1), 233–250. https://doi.org/10.4319/lo.2014.59.1.0233

Crookshanks, S., & Gilbert, R. (2008). Continuous, diurnally fluctuating turbidity currents in Kluane Lake, Yukon Territory. *Canadian Journal of Earth Sciences*, *45*(10), 1123–1138. https://doi.org/10.1139/E08-058

De Cesare, G., Schleiss, A., & Hermann, F. (2001). Impact of turbidity currents on reservoir sedimentation. *Journal of Hydraulic Engineering*, *127*(1), 6–16. https://doi.org/10.1061/(ASCE)0733-9429(2001)127:1(6)

De Lorenzis, L., & Düster, A. (2020). Modeling in engineering using innovative numerical methods for solids and fluids. In *CISM international centre for mechanical sciences* (Vol. 599). Springer International Publishing. https://doi.org/10.1007/978-3-030-37518-8

Farrell, G. J., & Stefan, H. G. (1988). Mathematical modeling of plunging reservoir flows. *Journal of Hydraulic Research*, *26*(5), 525–537. https://doi.org/10.1080/00221688809499191

Fischer, H. B., List, E., Koh, R., Imberger, J., & Brooks, N. (1979). *Mixing in inland and coastal waters*. Academic Press. https://doi.org/10.1016/C2009-0-22051-4

Fleenor, W. (2001). *Effects and control of plunging inflows on reservoir hydrodynamics and downstream releases*. Unpublished Ph.D. thesis. University of California. Retrieved from https://search.library.ucdavis.edu/permalink/01UCD_INST/9fle3i/alma990021089970403126

Garrett, B. (1960). *Hydrodynamics* (2nd ed.). Princeton University Press. Retrieved from https://press.princeton.edu/books/ebook/9781400877775/hydrodynamics

Gray, D. D., & Giorgini, A. (1976). The validity of the Boussinesq approximation for liquids and gases. *International Journal of Heat and Mass Transfer*, *19*(5), 545–551. https://doi.org/10.1016/0017-9310(76)90168-X

Härtel, C., Meiburg, E., & Necker, F. (2000). Analysis and direct numerical simulation of the flow at a gravity-current head. Part 1. Flow topology and front speed for slip and no-slip boundaries. *Journal of Fluid Mechanics*, *418*, 189–212. https://doi.org/10.1017/S0022112000001221

Hauenstein, W. (1982). Zuflussbedingte dichteströmungen in seen. Unpublished Ph.D. thesis. Retrieved from https://eth.swisscovery.slsp.ch/permalink/41SLSP_ETH/lshl64/alma990003139310205503

Hauenstein, W., & Dracos, T. (1984). Investigation of plunging density currents generated by inflows in lakes. *Journal of Hydraulic Research*, *22*(3), 157–179. https://doi.org/10.1080/00221688409499404

Hogg, C. A. R., Marti, C. L., Huppert, H. E., & Imberger, J. (2013). Mixing of an interflow into the ambient water of Lake Iseo. *Limnology and Oceanography*, *58*(2), 579–592. https://doi.org/10.4319/lo.2013.58.2.0579

Jasak, H. (2009). OpenFOAM: Open source CFD in research and industry. *International Journal of Naval Architecture and Ocean Engineering*, *1*(2), 89–94. https://doi.org/10.2478/IJNAOE-2013-0011

Johnson, T. R., Ellis, C. R., Farrell, G. J., & Stefan, H. G. (1987). Negatively buoyant flow in a diverging channel. II: 3-D flow field descriptions. *Journal of Hydraulic Engineering*, *113*(6), 731–742. https://doi.org/10.1061/(ASCE)0733-9429(1987)113:6(731)

Johnson, T. R., Ellis, C. R., & Stefan, H. G. (1989). Negatively buoyant flow in diverging Channel, IV: Entrainment and dilution. *Journal of Hydraulic Engineering*, *115*(4), 437–456. https://doi.org/10.1061/(ASCE)0733-9429(1989)115:4(437)

Johnson, T. R., Farrell, G. J., Ellis, C. R., & Stefan, H. G. (1987). Negatively buoyant flow in a diverging channel. I: Flow regimes. *Journal of Hydraulic Engineering*, *113*(6), 716–730. https://doi.org/10.1061/(ASCE)0733-9429(1987)113:6(716)

Kostaschuk, R., Nasr-Azadani, M. M., Meiburg, E., Wei, T., Chen, Z., Negretti, M. E., et al. (2018). On the causes of pulsing in continuous turbidity currents. *Journal of Geophysical Research: Earth Surface*, *123*(11), 2827–2843. https://doi.org/10.1029/2018JF004719

Lamb, M. P., McElroy, B., Kopriva, B., Shaw, J., & Mohrig, D. (2010). Linking river-flood dynamics to hyperpycnal-plume deposits: Experiments, theory, and geological implications. *The Geological Society of America Bulletin*, *122*(9–10), 1389–1400. https://doi.org/10.1130/B30125.1

Lee, H., & Yu, W. (1997). Experimental study of reservoir turbidity current. *Journal of Hydraulic Engineering*, *123*(6), 520–528. https://doi.org/10.1061/(ASCE)0733-9429(1997)123:6(520)

Mayeli, P., & Sheard, G. J. (2021). Buoyancy-driven flows beyond the Boussinesq approximation: A brief review. *International Communications in Heat and Mass Transfer*, *125*, 105316. https://doi.org/10.1016/j.icheatmasstransfer.2021.105316

Ooi, S. K., Constantinescu, G., & Weber, L. (2009). Numerical simulations of lock-exchange compositional gravity current. *Journal of Fluid Mechanics*, *635*, 361–388. https://doi.org/10.1017/S0022112009007599

Özgökmen, T. M., Fischer, P. F., Duan, J., & Iliescu, T. (2004). Three-dimensional turbulent bottom density currents from a high-order nonhydrostatic spectral element model. *Journal of Physical Oceanography*, *34*(9), 2006–2026. https://doi.org/10.1175/1520-0485(2004)034<2006:TTBDCF>2.0.CO;2

Parker, G., Fukushima, Y., & Pantin, H. M. (1986). Self-accelerating turbidity currents. *Journal of Fluid Mechanics*, *171*(1), 145. https://doi.org/10.1017/S0022112086001404

Parker, G., & Toniolo, H. (2007). Note on the analysis of plunging of density flows. *Journal of Hydraulic Engineering*, *133*(6), 690–694. https://doi.org/10.1061/(ASCE)0733-9429(2007)133:6(690)

Piton, V., Soulignac, F., Ulrich, L., Graf, B., Wynn, H. K., Blanckaert, K., & Barry, D. A. (2022). Tracing unconfined nearfield spreading of a river plume interflow in a large lake (Lake Geneva): Hydrodynamics, suspended particulate matter and associated fluxes. *Frontiers in Water*, *4*, 943242. https://doi.org/10.3389/frwa.2022.943242

Pope, E. L., Cartigny, M. J. B., Clare, M. A., Talling, P. J., Lintern, D. G., Vellinga, A., et al. (2022). First source-to-sink monitoring shows dense head controls sediment flux and runout in turbidity currents. *Science Advances*, *8*(20), eabj3220. https://doi.org/10.1126/sciadv.abj3220

Scheu, K. R., Fong, D., Monismith, S. G., & Fringer, O. B. (2018). Modeling sedimentation dynamics of sediment-laden river intrusions in a rotationally-influenced, stratified lake. *Water Resources Research*, *54*(6), 4084–4107. https://doi.org/10.1029/2017WR021533

Sequeiros, O. E. (2012). Estimating turbidity current conditions from channel morphology: A Froude number approach: Gravity flow estimation Froude approach. *Journal of Geophysical Research*, *117*(C4), C04003. https://doi.org/10.1029/2011JC007201

Sequeiros, O. E., Naruse, H., Endo, N., Garcia, M. H., & Parker, G. (2009). Experimental study on self-accelerating turbidity currents. *Journal of Geophysical Research*, *114*(C5), C05025. https://doi.org/10.1029/2008JC005149

Shin, J. O., Dalziel, S. B., & Linden, P. F. (2004). Gravity currents produced by lock exchange. *Journal of Fluid Mechanics*, *521*, 1–34. https://doi.org/10.1017/S002211200400165X

Singh, B., & Shah, C. R. (1971). Plunging phenomenon of density currents in reservoirs. *La Houille Blanche*, *1*, 59–64. https://doi.org/10.1051/lhb/1971005

Soulignac, F., Lemmin, U., Ziabari, S. M. H., Wynn, H. K., Graf, B., & Barry, D. A. (2021). Rapid changes in river plume dynamics caused by advected wind-driven coastal upwelling as observed in Lake Geneva. *Limnology and Oceanography*, *66*(8), 3116–3133. https://doi.org/10.1002/lno.11864

Spigel, R. H., Howard-Williams, C., Gibbs, M., Stephens, S., & Waugh, B. (2005). Field calibration of a formula for entrance mixing of river inflows to lakes: Lake Taupo, North Island, New Zealand. *New Zealand Journal of Marine & Freshwater Research*, *39*(4), 785–802. https://doi.org/10.1080/00288330.2005.9517353

Stefan, H. G., & Johnson, T. R. (1989). Negatively buoyant flow in diverging channel. III: Onset of underflow. *Journal of Hydraulic Engineering*, *115*(4), 423–436. https://doi.org/10.1061/(ASCE)0733-9429(1989)115:4(423)

Tominaga, Y., & Stathopoulos, T. (2007). Turbulent Schmidt numbers for CFD analysis with various types of flowfield. *Atmospheric Environment*, *41*(37), 8091–8099. https://doi.org/10.1016/j.atmosenv.2007.06.054

Tseng, C. Y., & Chou, Y. J. (2018). Nonhydrostatic simulation of hyperpycnal river plumes on sloping continental shelves: Flow structures and nonhydrostatic effect. *Ocean Modelling*, *124*, 33–47. https://doi.org/10.1016/j.ocemod.2018.02.003

Weller, H. G., Tabor, G., Jasak, H., & Fureby, C. (1998). A tensorial approach to computational continuum mechanics using object-oriented techniques. *Computers in Physics*, *12*(6), 620. https://doi.org/10.1063/1.168744

Wright, L. D., Yang, Z. S., Bornhold, B. D., Keller, G. H., Prior, D. B., & Wiseman, W. J. (1986). Hyperpycnal plumes and plume fronts over the Huanghe (Yellow River) delta front. *Geo-Marine Letters*, *6*(2), 97–105. https://doi.org/10.1007/BF02281645

References From the Supporting Information

Bonamy, C., Chauchat, J., Augier, P., Mathieu, A., Clemencot, Q., Chassagne, R., et al. (2020). Fluiddyn/fluidfoam: Release v0.2.3 (v0.2.3). https://doi.org/10.5281/zenodo.6453090

Kim, W., & Menon, S. (1995). A new dynamic one-equation subgrid-scale model for large eddy simulations. In *33rd aerospace sciences meeting and exhibit* (p. 356). https://doi.org/10.2514/6.1995-356

Nezu, I., & Nakagawa, H. (1993). *Turbulence in open-channel flows*. IAHR, A.A. Balkema. Netherlands. https://doi.org/10.1201/9780203734902

Poletto, R., Craft, T., & Revell, A. (2013). A new divergence free synthetic eddy method for the reproduction of inlet flow conditions for LES. *Flow, Turbulence and Combustion*, *91*(3), 519–539. https://doi.org/10.1007/s10494-013-9488-2